RSC Advances

PAPER

View Article Online
View Journal | View Issue

Cite this: *RSC Adv.*, 2021, **11**, 20850

Polymer encapsulated clinical ICG nanoparticles for enhanced photothermal therapy and NIR fluorescence imaging in cervical cancer†

Shuang Chen,[a] Lijun Zhu,[b] Zhong Du,[a] Rong Ma,[a] Ting Yan,[b] Gulinigaer Alimu,[b] Xueliang Zhang,[b] Nuernisha Alifu *[b] and Cailing Ma*[a]

Photothermal therapy (PTT) is a popular tumor therapy method, which is based on efficient photothermal nanoagents (PTNs). Clinical Indocyanine Green (ICG), as a Food and Drug Administration (FDA) approved agent, is an often-used PTN, meanwhile it is also a good near-infrared (NIR) fluorescence contrast agent. However, the further applications of ICG in biomedical fields are limited due to its poor stability. In this study, ICG was encapsulated by the amphiphilic polymer poly(styrene-*co*-maleic anhydride) (PSMA) to form ICG@PSMA nanoparticles. Furthermore, optical and thermal characteristics of ICG@PSMA nanoparticles were studied in detail. Strong NIR fluorescence and excellent photothermal properties of ICG@PSMA nanoparticles under 808 nm laser irradiation were measured. Besides, favorable biocompatibility of ICG@PSMA nanoparticles was demonstrated on a human cervical cancer cell line (HeLa) *via* cell viability studies. Hence, ICG@PSMA nanoparticles were further applied to enhanced PTT of living HeLa cells under 808 nm excitation, and a high PTT efficiency of ~70% was obtained. The novel ICG nanoparticles as a promising PTT nanoplatform could offer an opportunity for further tumour treatments.

Received 13th April 2021
Accepted 4th June 2021

DOI: 10.1039/d1ra02875h

rsc.li/rsc-advances

1. Introduction

Cervical cancer is a growing and significant threat for woman's health.[1] The commonly used treatment methods for cervical cancer include surgery, radiotherapy, chemotherapy *etc*.[2] However, these treatments still have some drawbacks and side effects. For example, surgical excision lacks targeting specificity, radiotherapy may damage healthy tissues,[3] and chemotherapy has low selectivity for cervical cancer.[4] Therefore, it is necessary to develop efficient and non-invasive treatment methods for cervical cancer.

Photothermal therapy (PTT) is a promising tumour therapy method.[5–7] During the photothermal process, the excitation light is absorbed by photothermal nanoagents (PTN) and converted into heat (more than 42 °C) for tumour ablation.[8–11] In recent years, nanoprobe-assisted PTT has attracted wide attention in biomedicine, because of its light-induced heating with no damage to the normal tissues.[12,13] PTN are one key reason for effective PTT.[14–16] To achieve high PTT efficiency, PTN with biocompatible, NIR emissive and well photothermal properties are favorable.[17–19]

Indocyanine Green (ICG) is a clinically relevant contrast agent which is approved by the Food and Drug Administration (FDA).[20,21] Over the past few years, ICG has been widely used in various biomedical applications, such as cardiac output measurement, liver function monitoring, and ophthalmic angiography.[22,23] Besides, bioimaging application, ICG have also been used for PTT because of its advantages of high photothermal conversion efficiency under light irradiation.[24,25] Under laser irradiation, the ICG also produces photodynamic (PDT) effects, therefore PDT and PTT are often combine used.[26–29] Nevertheless, researchers were more inclined to study ICG-based PTT since ICG produces stronger photothermal effect. Besides, the poor optical and thermal stability of ICG as PTN limited its further applications.[30] To overcome these limits, ICG is commonly encapsulated into nanoparticles (NPs) under the condition that fluorescence of ICG is not quenched.[31–34] For example, Liu *et al.* developed PLGA-ICG-R837 NPs, and used the NPs for near-infrared laser-triggered photothermal ablation of primary tumours.[35] Cai *et al.* reported cancer cell membrane-coated NPs with an ICG/poly (lactic-*co*-glycolic acid) (PLGA) core and cancer cell membrane shell (ICNPs), which serve as a bionic nanoplatform for cancer-targeted imaging and phototherapy.[36] Lin *et al.* successfully designed Mo@Fe-ICG/Pt nanocomposites which remarkably enhanced anti-tumor efficacy of combined PTT.[37]

Different types of polymers encapsulated ICG have exhibited great advantages in biomedical applications. ICG encapsulated

[a]*State Key Laboratory of Pathogenesis, Prevention, and Treatment of High Incidence Diseases in Central Asia/Department of Gynecology, The First Affiliated Hospital of Xinjiang Medical University, Urumqi, 830054, China. E-mail: hymcl@sina.com*

[b]*State Key Laboratory of Pathogenesis, Prevention and Treatment of High Incidence Diseases in Central Asia/School of Medical Engineering and Technology, Xinjiang Medical University, Urumqi, 830054, China. E-mail: nens_xjmu@126.com*

† Electronic supplementary information (ESI) available. See DOI: 10.1039/d1ra02875h

by the quantum dots tend to have a higher quantum yield, which was mainly used to enhance fluorescence in bioimaging.[38] Nanoflake was often conducted to drug delivery due to smaller sizes.[39] While nanocrystals encapsulate ICG were more effective in enhancing photothermal.[27–29] Studies have shown that the polymer encapsulated clinical ICG nanoparticles can not only increase the stability of nanoparticles, but also could enhance PDT/PTT effect, meanwhile strengthen biocompatibility of the NPs with negligible toxicity.[27–29] Poly(styrene-*co*-maleic anhydride) (PSMA) is an amphiphilic polymer[40] and often selected as encapsulation matrix for organic dyes to increase their chemical stability and biocompatibility.[41–45] In addition, PSMA has been used clinically and its covalent binding to proteins has been studied.[43,46,47] However, the reports of PSMA coated clinical ICG still rare.

In this study, we used clinical ICG and encapsulated it with PSMA by self-assembly method to form ICG@PSMA NPs. ICG@PSMA NPs showed strong NIR fluorescence, well biocompatibility, low toxicity and excellent photothermal ability. Further, ICG@PSMA NPs were utilized as NIR fluorescence imaging agents for the cervical cancer cell. Also, ICG@PSMA NPs showed good PTT property in cervical cancer cells as PTN under 808 nm laser irradiation with PTT efficiency of ~70%. Besides, ICG@PSMA NPs[27–29] have great potentials in other different types of cancer. Therefore, ICG@PSMA NPs have great potentials as PTN for tumor therapy, and our results can provide a good basis for following *in vivo* experiments.

2. Experimental section

2.1 Materials and animals

Indocyanine Green for Injection (ICG) was purchased from Hangzhou Aoya Biotechnology Co., Ltd. Poly(styrene-co-maleic anhydride) (PSMA) and Tetrahydrofuran (THF) were purchased from Shanghai Aladdin Biochemical Technology Co.,Ltd. High glucose Dulbecco's Modified Essential Medium (DMEM), Trypsin and Phosphate-balanced saline (PBS) were bought from Shanghai Hyclone Co., Ltd. Fetal Bovine Serum (FBS) were purchased from Shanghai Kanglang Biotechnology Co., Ltd. Cell Counting Kit-8 (CCK-8) and 4′,6-Diamidino-2-phenylindole (DAPI) Staining Solution were bought from Biosharp Co., Ltd. Annexin V-FITC apoptosis detection kit were purchased from BD Biosciences Pharmingen Co.,Ltd. Deionized (DI) water was used in all experimental process.

The rats (female, 200 g) and Kunming (KM) mice (female, 20 g) were purchased and fed in Animal Experiment Center, Xinjiang Medical University. All animal procedures were approved by the Ethics Committee for Animal Experiments of Xinjiang Medical University. The aforementioned mice were raised and bred at the Experimental Animal Center of Xinjiang Medical University.

2.2 Synthesis of ICG@PSMA nanoparticles (NPs)

Synthesis approaches of polymer encapsulated clinical ICG can be categorized into top-down and bottom-up methods.[48] Different strategies and methods of preparation produce distinct nano-morphologies appropriate for various biomedical applications. The top-down ways can usually produce nanoparticles with relatively smaller size in diameter[48] so that it can be better used in biomedicine. Accordingly, ICG@PSMA NPs were synthetised by top-down approach. ICG@PSMA NPs were prepared by a self-assembly method according to previous work.[42] The detailed experimental steps are as follows: 1 mg ICG was dissolved into DI water to make stock solution A (200 μg mL^{-1}). A similar method was used to make stock solution B (PSMA in THF, 1 mg mL^{-1}). Then, 1 mL stock solution A was added into different volumes (200 μL, 100 μL, 67 μL, and 50 μL) of solution B to produce various solution mixtures. Then each mixture was quickly formed carboxyl functionalized NPs under ultrasonic condition, and then placed in the water bath to remove residual THF. During the formation process of ICG@PSMA NPs, the maleic anhydride units of PSMA molecules were hydrolyzed in the aqueous environment and formed carboxyl groups. The as-synthesized ICG@PSMA NPs were dialyzed in water (5 KD, 24 h) to remove free ICG and PSMA. Subsequently, the ICG@PSMA NPs were collected in the supernatant by filtration with a 0.22 μm filter to remove the precipitate impurities.

2.3 Characterization of ICG@PSMA NPs

The morphology and structure of ICG@PSMA NPs were characterized by the transmission electron microscope (TEM, JEM-1230, JEOL, Ltd, Japan). The dynamic diameter and distribution of the ICG@PSMA NPs were characterized with dynamic light scattering (DLS) method at 25 °C using a Zetasizer Nano ZS-90 (Malvern, UK). The absorption spectra of the ICG@PSMA NPs were obtained from a Lambda 750S UV/vis/NIR spectrophotometer (PerkinElmer). The fluorescence spectra of the ICG@PSMA NPs were measured with a Duetta Fluorescence and Absorbance spectrofluorophotometer (HORIBA Canada). The Maestro™ *in vivo* fluorescence imaging system (Perkin Elmer) and the confocal laser scanning microscope (CLSM, Nikon ECLIPSE Ti, Japan) were employed to analyze the NIR fluorescence property of ICG@PSMA NPs.

2.4 Cell culture and cell toxicity analysis

The human cervical cancer cell line HeLa cells were obtained from American Type Culture Collection (ATCC) and cultured with DMEM containing 10% FBS and 1% antibiotics (penicillin–streptomycin) at 37 °C with a 5% CO_2 humidified atmosphere. When the cells are overgrown with 80%, 1 : 2 or 1 : 3 passage is carried out as needed.

The CCK-8 experiment was employed to evaluate the viability of HeLa cells after 24 hours incubation of free ICG and ICG@PSMA NPs at different concentrations. HeLa cells were seeded into 96-well plates with 5×10^3 cells per well (200 μL cell culture medium) and cultured for 24 hours (5% CO_2, 37 °C). Then, a fresh DMEM culture medium that contained free ICG and ICG@PSMA NPs at different concentrations (0, 0.8, 1.6, 3.2, 6.3, 12.5, 25 and 50 μg mL^{-1} of final ICG concentrations) was added to replace the old culture medium. After 24 hours incubation, a standard CCK-8 assay was used to evaluate the relative cytotoxicity.

2.5 Photothermal properties analysis of ICG@PSMA NPs

To measure the photothermal property of ICG@PSMA NPs, different laser power densities were utilized. In detail, the experiment was divided into five groups, labelled as A, B, C, D, E. The concentration of ICG@PSMA NPs in aqueous dispersion in each

group was 200 μg mL^{-1} (counted by ICG content, water as solvent), and each solution had a volume of 500 μL. The ICG@PSMA NPs in aqueous dispersion, under 80 mW cm^{-2} laser irradiation in group A, 160 mW cm^{-2} laser irradiation in group B, 320 mW cm^{-2} laser irradiation in group C, 640 mW cm^{-2} laser irradiation in group D, and 900 mW cm^{-2} laser irradiation in group E for 12 minutes. The temperature changes were monitored by the infrared thermal imaging camera (FOTRIC, Shanghai Heat Image Technology Co., Ltd) and recorded at every 30 seconds.

Further, under the same excitation power density, the temperatures of ICG@PSMA NPs in aqueous dispersion of different concentrations (counted by ICG content, with water as solvent) were analyzed. In detail, the samples were divided into five groups, labelled as I, II, III, IV, V. Each group was irradiated under a 640 mW cm^{-2} laser for 12 minutes and each solution had a volume of 500 μL. The ICG@PSMA NPs in aqueous dispersion concentration of group I was 3.125 μg mL^{-1}, group II was 6.25 μg mL^{-1}, group III was 12.5 μg mL^{-1}, group IV was 50 μg mL^{-1}, and group V was 200 μg mL^{-1}. The temperature changes of each group under laser irradiation were recorded at every 30 seconds. The temperature change of DI water under the same conditions was monitored and recorded as a control group.

Then the photothermal stability of ICG@PSMA NPs was studied. The temperature changes of five continuous cold and hot cycles (laser on/off) for ICG@PSMA NPs in aqueous were analyzed. Based on the results of previous experiments, the concentration of 200 μg mL^{-1} and excitation power density of 640 mW cm^{-2} were adopted. The ICG@PSMA NPs in aqueous dispersion was exposured to laser irradiation for 12 minutes and then cooled naturally to room temperature. The temperature changes of each group under laser irradiation were recorded at every 30 seconds. As a comparison, the same detection for free ICG in aqueous under the same conditions was did.

2.6 NIR confocal fluorescence microscopic imaging of HeLa cells

To verify the NIR fluorescence of the ICG@PSMA NPs at the cell level, the cells were image under CLSM. Experimental group was seeded with 10^5 HeLa cells in a confocal culture dish (35 mm in diameter). HeLa cells were incubated for 18 hours (5% CO_2, 37 °C), and then replaced the old medium with the same amount of fresh medium. Afterwards, the cells were divided into following six groups: (1) control, (2) ICG (50 μg mL^{-1}), (3) ICG (100 μg mL^{-1}), (4) ICG@PSMA NPs (50 μg mL^{-1}, counted by ICG content) and (6) ICG@PSMA NPs (100 μg mL^{-1}). After 2 hours of incubation, the medium of each group was discarded and the cells were washed with 1 × PBS (pH = 7.4) for three times. Then, the cells were stained with DAPI for 5 minutes, and then washed three times with 1× PBS. The cellular uptake of drugs and NIR fluorescence were observed by the fluorescent microscope *via* blue (DAPI) and red (ICG) channels under 480 nm/640 nm excitation and detected by 810–1000 nm emission, respectively.

2.7 Photothermal therapy analysis of living cells

NIR fluorescence imaging guided PTT analysis was carried out and the PTT efficiency in living cells was studied. Briefly, HeLa cells were seeded into a cell culture dish (35 mm in diameter) that was equipped with glass (0.13 mm in thickness) at the bottom and incubated for 18 hours (5% CO_2, 37 °C). The cells were divided into four groups as follows: (1) control (without any treatments), (2) treated with ICG@PSMA NPs (50 μg mL^{-1}, counted by ICG content), (3) treated with laser only, and (4) treated with both ICG@PSMA NPs (50 μg mL^{-1}) and laser. After incubated by ICG@PSMA NPs for 2 hours, the cells were stained with the Annexin V-FITC for 10 minutes. Then, the cells were irradiated by 808 nm laser irradiation (900 mW cm^{-2}) for 3 minutes. Then fluorescence images were collected for the cells *via* green (FITC) and red (ICG) channels under 530 nm/640 nm excitation and detected by 810–1000 nm emission, respectively.

Further, the PTT cell apoptosis of ICG@PSMA NPs were evaluated by Flow Cytometry. HeLa cells were seeded in 6-well plates at a density of 3×10^5 cells per well. After 24 hours incubation, the cells were divided into four groups: (1) control, (2) Laser only, (3) ICG@PSMA NPs (50 μg mL^{-1}), and (4) ICG@PSMA NPs (50 μg mL^{-1}) and Laser. After 2 hours of incubation by ICG@PSMA NPs, laser irradiation was used (808 nm laser irradiation at a power density of 900 mW cm^{-2} for 8 minutes). Then, the cells were incubated at 37 °C with 5% CO_2 and 95% air for 12 hours. Afterwards, all of the cells were washed with PBS, digested by trypsin, and collected by centrifugation. After being further washed with PBS for 2 times, the cells were re-suspended in 0.5 mL of annexin binding buffer. After that, all cells were stained in PI and Annexin-V-FITC containing binding buffer for 15 minutes and finally detected by flow cytometry (BD LSRII, FACS Calibur).

2.8 Biosafety assays

Biocompatibility of ICG@PSMA NPs was evaluated by the hemolysis test. First, blood samples from healthy rat were collected into heparinized tube and red blood cells (RBCs) were separated by centrifugation at 1000 rpm for 10 minutes. The collected RBCs were washed three times with 1× PBS. For positive and negative controls, 2% RBCs suspensions were made with DI water and PBS separately. Next, all samples were diluted with PBS at a concentration of ICG@PSMA NPs at 6.25, 12.5, 25, 50 and 100 μg mL^{-1} and were incubated with 2% of RBCs (1.5 mL) at 37 °C for 3 hours. Further, to determine the effect of NIR, the samples was irradiated with NIR radiation at 900 mW cm^{-2} for 8 minutes. After that, all treated samples were centrifuged at 1000 rpm for 10 minutes to compare the clarity of the samples.

Then, the biosafety effect of ICG@PSMA NPs *in vivo* was ascertained. Six healthy female KM mice were intravenously injected with ICG@PSMA NPs at a dose of 10 μg kg^{-1} and sacrificed at 24 hours and 3 days after injection. Major organs from the treated mice were collected for hematoxylin and eosin (H&E) staining according to the standard protocol and examined using an inverted digital microscope (Leica).

3. Results and discussion

3.1 Synthesis and characterization of ICG@PSMA NPs

The fabrication procedure of ICG@PSMA NPs was schematically illustrated in Fig. 1(a), which was facile and convenient. The

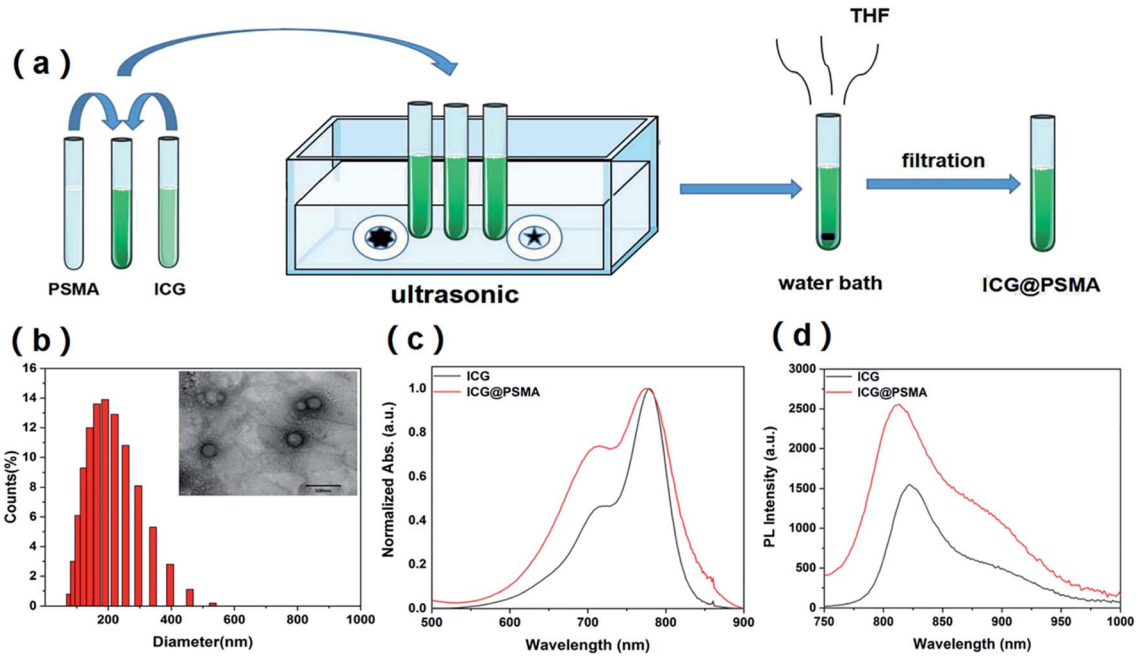

Fig. 1 (a) The scheme of preparation of ICG@PSMA NPs. (b) DLS measurement of ICG@PSMA NPs (insert: TEM images of ICG@PSMA NPs, scale bar: 500 nm). (c) The absorption and (d) fluorescence spectra of free ICG molecules (gray line) and ICG@PSMA NPs (red line) in water (pH = 7.4).

maleic anhydride units of PSMA molecules were hydrolysed in the aqueous environment and generated carboxyl groups on the surface of NPs (Scheme 1). The ICG@PSMA NPs were dispersed clearly and stably in the water. The morphology and hydrodynamic size distribution of as-synthesized ICG@PSMA NPs (with a weight ratio of ICG : PSMA = 3 : 1) were characterized by TEM and dynamic light scattering (DLS). As shown in the TEM image (Fig. 1(b) and S1†), the obtained ICG@PSMA NPs exhibit a uniformly spherical structure with an average diameter of ~180 nm. The DLS analysis is also used conform the size distribution of ICG@PSMA NPs (~180 nm). In addition, there was almost no change of hydrodynamic diameter of nanoparticles for 9 consecutive days (Fig. S2†), indicating the high stability of ICG@PSMA NPs in aqueous solution.

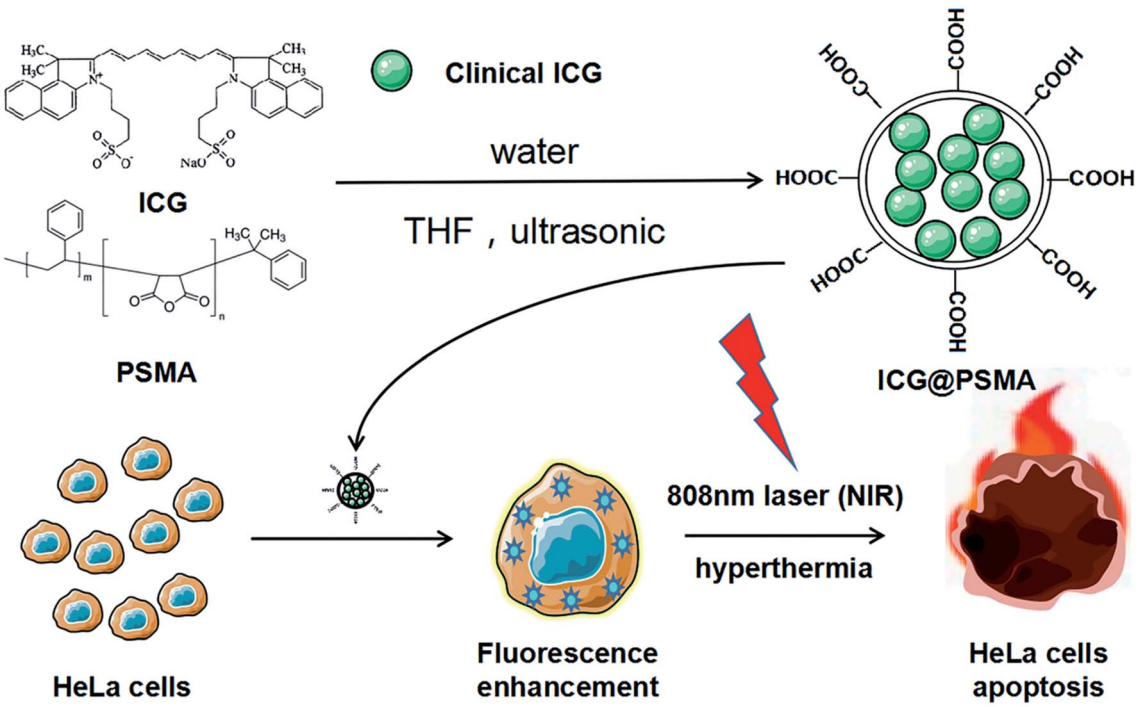

Scheme 1 Schematic illustration of the synthesis process ICG@PSMA NPs and PTT effect.

We further evaluated the absorption and the fluorescence spectrum of ICG and ICG@PSMA NPs in aqueous dispersion to verify the molecular interaction between ICG and PSMA. As shown in Fig. 1(c), ICG (gray line) and ICG@PSMA NPs (red line) exhibited strong absorption peak at ~780 nm. Therefore, the prepared ICG@PSMA NPs were suitable for NIR excitation of 808 nm laser. Free ICG in aqueous dispersion showed two characteristic absorption peaks at 719.5 nm and 779.5 nm, which shifted to 715 nm and 775 nm in the presence of PSMA. The slightly blue-shift of the absorption peak indicate an interaction between ICG molecule and the PSMA molecule. The interaction between two molecules indicates the successful introduction of ICG into the PSMA-based nanoparticles. Then the fluorescence spectra of ICG and ICG@PSMA NPs was measured as shown in Fig. 1(d). ICG molecules and ICG@PSMA NPs showed their fluorescence peak at ~820 nm. Most of the emitted light in the NIR band, which can produce NIR strong fluorescence signal. Thus, the ICG@PSMA NPs in aqueous dispersion emitted stronger NIR emission than free ICG molecules under same ICG concentration, which attributes to the intermolecular interaction between ICG molecule and PSMA molecule. Therefore, PSMA was suitable to formulate ICG@PSMA NPs by an intermolecular interaction, which facilitated the formation of the ICG@PSMA NPs for biomedical application. The loading efficiency (LE) of ICG were further studied, which was calculated *via* UV *vis* spectrophotometric method.[28] The loaded ICG dose in ICG@PSMA NPs was determined by the absorption value. The calculation formula was as follows:[28]

$$\mathrm{LE}(\%) = \frac{\mathrm{ICG_{loaded}}}{\mathrm{Weight_{NPs}}} \times 100\%$$

Then, the LE of ICG in ICG@PSMA NPs was calculated to be 6.2%, which is comparable to many other different types of polymer encapsulated ICG nanoparticles, such as H-PMOF (17.4%),[27] CMCh-BAPE-RGD@ICG Nanoparticles (7.5%),[28] PLGA-ICG-R848 NPs ((0.82 ± 0.03)%).[49]

3.2 *Ex vivo* NIR fluorescence imaging and cytotoxicity analysis

Free ICG and ICG@PSMA NPs in aqueous dispersion under daylight were shown in Fig. 2(a) (left). ICG@PSMA NPs in aqueous dispersion is as green as ICG, clear and transparent, slightly darker than the ICG. Further, NIR fluorescence property of ICG@PSMA NPs, ICG in aqueous dispersion (200 μg mL^{-1}) and ICG@PSMA NPs in aqueous dispersion (200 μg mL^{-1}, counted by ICG content) were analyzed under an *in vivo* fluorescence imaging system (745 nm laser excitation, 840 nm emission). As shown in Fig. 2(a) (right), the ICG@PSMA NPs in aqueous dispersion showed stronger fluorescence at the same imaging condition. The improved NIR fluorescence emission property is further confirmed with the fluorescence imaging of free ICG and ICG@PSMA NPs in aqueous dispersion samples (200 μg mL^{-1}, counted by ICG content) under the CLSM (λ_{em} = 800–1000 nm, λ_{ex} = 640 nm (ICG)) (Fig. 2(b)). In order to evaluate biocompatibility of ICG@PSMA NPs, cell toxicity of HeLa cells was conducted at a serial concentration of ICG@PSMA NPs. As shown in Fig. 2(c), more than 80% of the cells had survived after being treated at the tested concentrations. The results suggested that free ICG and ICG@PSMA NPs were nontoxic to cells.

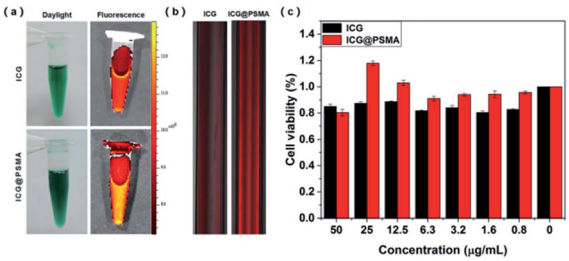

Fig. 2 (a) Free ICG and ICG@PSMA NPs in aqueous dispersion under the irradiation of daylight (left) and *in vivo* fluorescence imaging system (right, λ_{em} = 800–1000 nm, λ_{ex} = 745 nm). (b) The fluorescence imaging of free ICG and ICG@PSMA NPs in aqueous dispersion (200 μg mL^{-1}, counted by ICG content) under the confocal fluorescence microscope (λ_{em} = 800–1000 nm, λ_{ex} = 640 nm). (c) Cytotoxicity of HeLa cells after incubation with free ICG and ICG@PSMA NPs at different concentrations for 24 hours. Data are expressed as mean ± S.D. (n = 3 in each concentration).

3.3 Photothermal properties of ICG@PSMA NPs

Efficient photothermal performance is an important condition to ensure the therapeutic efficacy of a PTN. Then photothermal properties of ICG@PSMA NPs in aqueous dispersion under the 808 nm irradiation were further explored, as presented in Fig. 3. First, the photothermal performance of ICG@PSMA NPs in aqueous dispersion was evaluated at different irradiation power density. As shown in Fig. 3(a) and S3,† the photothermal

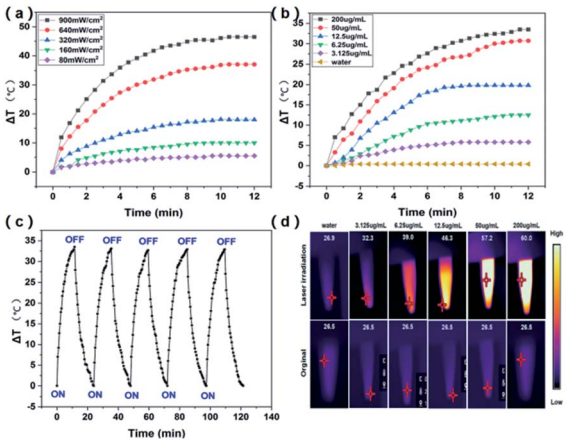

Fig. 3 (a) Temperature elevation of ICG@PSMA NPs in aqueous dispersion (200 μg mL^{-1}) under different power densities. (b) Temperature elevation of ICG@PSMA NPs in aqueous dispersion at different concentrations (808 nm excitation, 640 mW cm^{-2}) (c) heating/cooling curves of ICG@PSMA NPs in aqueous dispersion (200 μg mL^{-1}, 808 nm excitation, 640 mW cm^{-2}) for 5 repeated irradiation cycles. (d) Thermal Imaging of ICG@PSMA NPs in aqueous dispersion at different concentrations (808 nm excitation, 640 mW cm^{-2}).

performance of ICG@PSMA NPs in aqueous dispersion (200 μg mL^{-1}) was dependent on the irradiation power density. The temperature of ICG@PSMA NPs in aqueous dispersion increased by 46.1 °C (Fig. S3†) with the power density at 900 mW cm^{-2} after 12 minutes irradiation.

In addition, the temperature change of ICG@PSMA NPs in aqueous dispersion by controlling the ICG concentration (0, 3.125, 6.25, 12.5, 50, 200 μg mL^{-1}) at a constant power intensity (808 nm excitation, 640 mW cm^{-2}) were evaluated (Fig. 3(b)). The corresponding thermal imaging were conducted in Fig. 3(d). As expected, the increase of ICG concentration resulted in a faster increase of heat (Fig. 3(b) and (d)). At the ICG concentration of 200 μg mL^{-1}, the temperature of ICG@PSMA NPs in aqueous dispersion quickly risen to 33.5 °C (Fig. 3(d)). In contrast, the temperature of DI water almost unchanged under the same NIR irradiation condition.

Then the photothermal stability of ICG@PSMA NPs was studied. As shown in Fig. S4,† the highest temperature of free ICG in aqueous dispersion (200 μg mL^{-1}) gradually decreased after each cycle of irradiation, indicating the rapid decline of its photothermal heating capability probably because of the serious photo-bleaching of free ICG after laser irradiation. In marked contrast, the 5-cyclical laser irradiations (on and off) were also conducted under 808 nm (640 mW cm^{-2} (Fig. 3(c))). As displayed in Fig. 3(c), the ICG@PSMA NPs in aqueous dispersion (200 μg mL^{-1}) did not show any visible decay during the observation period. The temperature change was reproducible which suggests the superb photothermal stability of ICG@PSMA NPs in aqueous dispersion.

Furthermore, the photothermal conversion efficiency of free ICG and ICG@PSMA NPs were measured to demonstrate the photothermal conversion capability of them. According to the method reported by Yikai[50] the value was calculated as following:

$$\eta = \frac{M_D C_D (T_{max} - T_{max,water})}{\tau_s I \left(1 - 10^{-A_{808}}\right)} \times 100\%$$

where M_D is the mass of products, C_D is the heat capacity of solvent, T_{max} and T_{max}, water are maximum equilibrium temperature for NPs solution and water, I is the incident laser power, and A_{808} is the absorbance of the NPs at 808 nm. The η value of ICG@PSMA NPs was calculated as 33.2% (Fig. S5†), which was significantly higher than free ICG ($\eta = 14.5$, Fig. S6†). Besides, the η value of ICG@PSMA NPs is comparable to most ICG encapsulated by other types of polymer nanoparticles, such as mPEG-ACA-ICG (20.81%),[51] MINPs (35%),[52] ICG-CD (30.25%).[38] These results showed that the ICG@PSMA NPs were excellent photothermal reagents and could be a good candidate for PTT.

3.4 NIR confocal fluorescence microscopic imaging

Cell uptake ability of NPs is crucial for the PTT treatment. HeLa cells were incubated with free ICG (50, 100 μg mL^{-1}) and ICG@PSMA NPs (50, 100 μg mL^{-1}, counted by ICG concentration) for 2 hours. Then, the cells were stained with DAPI (blue color). Finally, the cells were imaged by the CLSM with 640 nm laser excitation for ICG and 405 nm laser excitation for DAPI. As shown in Fig. 4(a), the NIR fluorescence of the ICG and ICG@PSMA NPs (red colour) was observed within the cells, indicating the efficient internalization by the cells. Besides, the fluorescence of cells treated with free ICG was weaker than ICG@PSMA NPs. In contrast, no fluorescence was observed in the cells in the control group. The efficient uptake of ICG@PSMA NPs would contribute to the encapsulation PSMA, and the stronger fluorescence suggested ICG@PSMA NPs is superior to free ICG in fluorescence imaging. Besides, the fluorescence intensity of ICG@PSMA NPs depended on ICG concentration, as presented in Fig. S7.† The fluorescence quantitative analysis of images collected by the fluorescent microscope has further confirmed the viewpoint above (Fig. 4(b)). These results pointed out that ICG@PSMA NPs own excellent cellular uptaking ability.

3.5 Evaluation of PTT effect on living cells

The thermal ablation of tumor cells with PTT is a promising approach for anti-tumor therapy. Encouraged by the

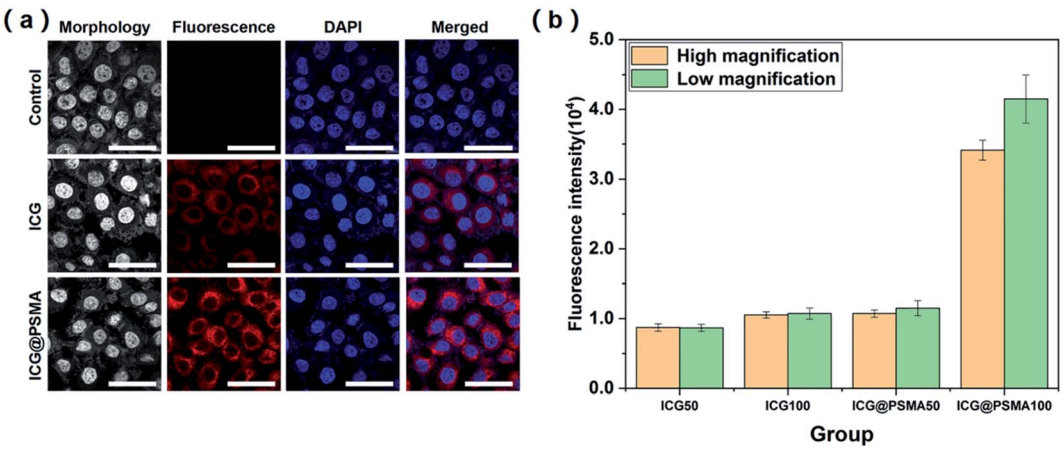

Fig. 4 (a) Fluorescent images of HeLa cells incubated with PBS, free ICG, and ICG@PSMA NPs under CLSM. Scale bar: 30 μm. λ_{em} = 800–1000 nm, λ_{ex} = 480 nm (DAPI), λ_{ex} = 640 nm (ICG). Images were obtained at a magnification of 20× objective. (b) Corresponding fluorescence quantitative analysis.

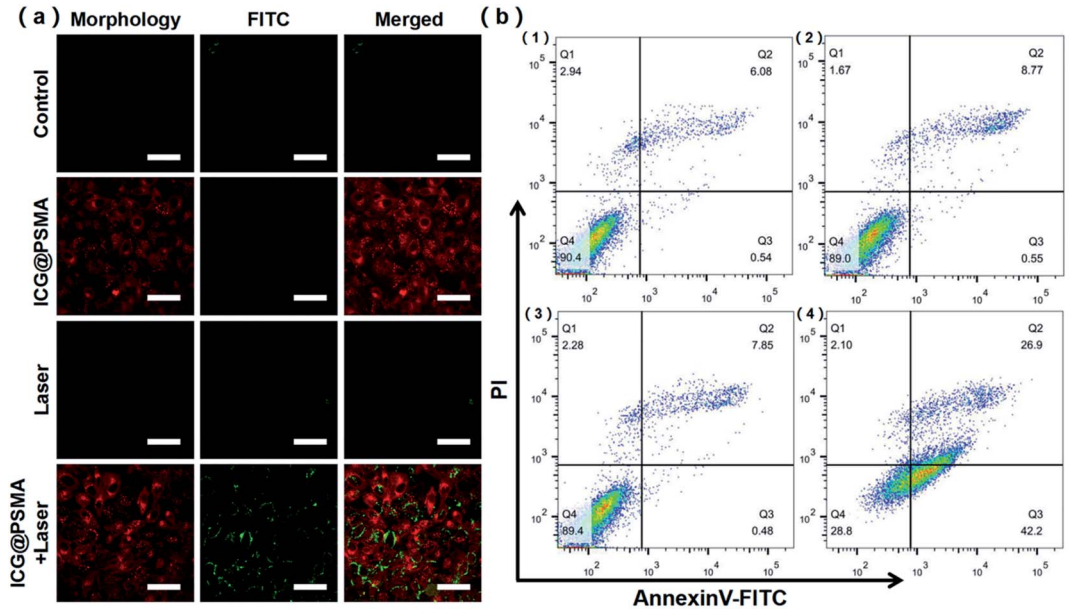

Fig. 5 (a) Fluorescence images of HeLa cells treated with DMEM, ICG@PSMA NPs, laser only and ICG@PSMA NPs and laser (808 nm laser irradiation at a power density of 900 mW cm^{-2} for 10 minutes) after stained by annexin V-FITC. Scale bar: 50 μm. λ_{ex} = 640 nm (ICG); λ_{ex} = 530 nm (FITC). Images were obtained at a 10 × objective. (b) Flow cytometric analysis by annexin V-FITC and PI staining: (1) control, (2) laser only, (3) ICG@PSMA NPs (50 μg mL^{-1}), (4) ICG@PSMA NPs (50 μg mL^{-1}) and Laser (808 nm laser irradiation at a power density of 900 mW cm^{-2} for 8 minutes).

outstanding photothermal property and cellular uptaking ability, the photothermal anti-tumor efficacy of ICG@PSMA NPs were carried out. The cytotoxicity of ICG@PSMA NPs with or without NIR irradiation were further analyzed. Live/dead fluorescent staining by Annexin V-FITC apoptosis detection kit has been adopted to assess the cell apoptosis and viability. The cells that start apoptosis emit green fluorescence after stained with the Annexin V-FITC. As shown in Fig. 5(a), little dead cells were observed in the ICG@PSMA NPs group that did not receive irradiation, indicating high biocompatibility of ICG@PSMA NPs. Compared to the laser group that exposed to the same laser intensities, ICG@PSMA NPs treated cancer cells displayed distinct cellular death, shown by the strong green fluorescence (Fig. 5(a)). These results suggested that ICG@PSMA NPs-mediated photothermal ablation was dependent on the laser irradiation.

To further survey the anticancer effect of ICG@PSMA NPs under 808 nm laser irradiation, the HeLa cells were double-labelled with Annexin V-FITC (fluorescein isothiocyanate) and PI (propidium iodide) for flow cytometry analysis. From the scatter plot in 4 quadrants which represent necrosis (left top, Q_1), late apoptosis (right top, Q_2), normal (left bottom, Q_4), and early apoptosis (right bottom, Q_3) (Fig. 5(b)), most cells were located in the viable region in the control group, laser only group, and ICG@PSMA NPs only group. Furthermore, the apoptotic rates are increased up to ~70% for the ICG@PSMA NPs hatched cells under 808 nm laser irradiation for 8 minutes (Fig. 5(b) and S8†). The apoptosis rate induced by ICG@PSMA NPs with 808 nm laser treatment was highest among all treatment groups. These results further suggested the excellent anticancer efficiency of ICG@PSMA NPs.

3.6 Biosafety study

Hemolytic assays are important to conduct for formulations intended for systemic use, especially for those nanopreparations requiring contact with the blood. A hemolysis assay was conducted to demonstrate the hemocompatibility of ICG@PSMA NPs in the formulations with and without NIR irradiation (Fig. S9†). As shown in the photographs (Fig. S9†), a 2% v/v suspension of rat RBCs was exposed with different concentrations (6.25, 12.5, 25, 50, and 100 μg mL^{-1}) of ICG@PSMA NPs in the formulations and no obvious hemolysis phenomenon was observed. The darker color of the high concentration group is due to the influence of drug color, and red blood cells are observed at the bottom of the centrifugal tube. In contrast, the rat RBCs exposed to DI water (+Ve control) had a significant hemolysis effect.

Then, we went on to further explore the biosafety of ICG@PSMA NPs *in vivo*. The biocompatibility of the ICG@PSMA NPs in living mice was evaluated through histological examinations on 24 hours and 3 days after intravenous injection with the ICG@PSMA NPs solution. H&E staining on the main organs of all mice demonstrated that no significant inflammation or damage was observed in all treatment groups (Fig. S10†). All above results strongly indicated satisfactory compatibility of ICG@PSMA NPs.

4 Conclusions

In this research, clinical ICG was used and encapsulated by PSMA to form ICG@PSMA NPs for NIR fluorescence imaging and PTT of HeLa cells. After encapsulation ICG with PSMA at

a reasonable weight ratio (ICG : PSMA = 3 : 1), the NIR fluorescence emission and photothermal stability of ICG were improved in both aqueous dispersion and in cells. Under 808 nm laser irradiation, the temperature of ICG@PSMA NPs in aqueous dispersion could rise to high temperature which could induce tumor cell death. The results of the cell experiment showed that ICG@PSMA NPs displayed strong hyperthermia-induced anticancer effect with PTT efficiency of 87.2%. Besides, the cytotoxicity results demonstrated that ICG@PSMA NPs causes no obvious toxicity on cells. In summary, our results suggested that ICG@PSMA NPs presented strong NIR fluorescence, well biocompatibility, low toxicity and excellent photothermal ability. We believe that ICG@PSMA NPs have great potentials in cervical tumor treatment in the future.

Conflicts of interest

The authors declare that they have no conflict of interest.

Acknowledgements

We gratefully acknowledge the National Natural Science Foundation of China (82060326 and 62035011), Fundamental Research Funds for the Central Universities and State Key Laboratory of Pathogenesis, Prevention and Treatment of High Incidence Diseases in Central Asia Fund (SKL-HIDCA-2019-3, SKL-HIDCA-2019-5), Natural Science Foundation of Xinjiang Uygur Autonomous Region (2020D01C151), Xinjiang Autonomous Region Collaborative Innovation Program(2019E0282).

Notes and references

1 H. Sung, J. Ferlay, R. L. Siegel, M. Laversanne, I. Soerjomataram, A. Jemal and F. Bray, *Ca-Cancer J. Clin.*, 2021, 1–41.
2 K. D. Miller, L. Nogueira, A. B. Mariotto, J. H. Rowland, K. R. Yabroff, C. M. Alfano, A. Jemal, J. L. Kramer and R. L. Siegel, *Ca-Cancer J. Clin.*, 2019, **69**, 363–385.
3 F. Kokka, A. Bryant, E. Brockbank, M. Powell and D. Oram, *Cochrane Database Syst. Rev.*, 2015, (4), CD010260.
4 D. Peer, J. M. Karp, S. Hong, O. C. Farokhzad, R. Margalit and R. Langer, *Nat. Nanotechnol.*, 2007, **2**, 751–760.
5 S. Chen, C. Xing, D. Huang, C. Zhou, B. Ding, Z. Guo, Z. Peng, D. Wang, X. Zhu, S. Liu, Z. Cai, J. Wu, J. Zhao, Z. Wu, Y. Zhang, C. Wei, Q. Yan, H. Wang, D. Fan, L. Liu, H. Zhang and Y. Cao, *Sci. Adv.*, 2020, **6**, 1–12.
6 Z. Xie, M. Peng, R. Lu, X. Meng, W. Liang, Z. Li, M. Qiu, B. Zhang, G. Nie, N. Xie, H. Zhang and P. N. Prasad, *Light Sci. Appl.*, 2020, **9**, 161.
7 Z. Xie, T. Fan, J. An, W. Choi, Y. Duo, Y. Ge, B. Zhang, G. Nie, N. Xie, T. Zheng, Y. Chen, H. Zhang and J. S. Kim, *Chem. Soc. Rev.*, 2020, **49**, 8065–8087.
8 Z. Zhang, J. Wang and C. Chen, *Adv. Mater.*, 2013, **25**, 3869–3880.
9 Y. Liu, K. Ai, J. Liu, M. Deng, Y. He and L. Lu, *Adv. Mater.*, 2013, **25**, 1353–1359.
10 Z. Zha, X. Yue, Q. Ren and Z. Dai, *Adv. Mater.*, 2013, **25**, 777–782.
11 M. Wu, W. Le, T. Mei, Y. Wang, B. Chen, Z. Liu and C. Xue, *Int. J. Nanomed.*, 2019, **14**, 4431–4448.
12 L. Cheng, K. Yang, Q. Chen and Z. Liu, *ACS Nano*, 2012, **6**, 5605–5613.
13 Y. Cai, W. Si, W. Huang, P. Chen, J. Shao and X. Dong, *Small*, 2018, **14**, e1704247.
14 M. Yang, J. Deng, H. Su, S. Gu, J. Zhang, A. Zhong and F. Wu, *Mater. Chem. Front.*, 2021, **5**, 406–417.
15 F. Wu, L. Yue, K. Cheng, J. Chen, K. L. Wong, W. K. Wong and X. Zhu, *ACS Biomater. Sci. Eng.*, 2020, **6**, 5230–5239.
16 F. Wu, L. Chen, L. Yue, K. Wang, K. Cheng, J. Chen, X. Luo and T. Zhang, *ACS Appl. Mater. Interfaces*, 2019, **11**, 21408–21416.
17 E.-K. Lim, T. Kim, S. Paik, S. Haam, Y.-M. Huh and K. Lee, *Chem. Rev.*, 2015, **115**, 327–394.
18 M. Luo, T. Fan, Y. Zhou, H. Zhang and L. Mei, *Adv. Funct. Mater.*, 2019, **29**, 1–19.
19 Z. Tang, N. Kong, J. Ouyang, C. Feng, N. Y. Kim, X. Ji, C. Wang, O. C. Farokhzad, H. Zhang and W. Tao, *Matter*, 2020, **2**, 297–322.
20 V. L. Dzurinko, A. S. Gurwood and J. R. Price, *Optometry*, 2004, **75**, 743–755.
21 W. de Graaf, S. Häusler, M. Heger, T. M. van Ginhoven, G. van Cappellen, R. J. Bennink, G. A. Kullak-Ublick, R. Hesselmann, T. M. van Gulik and B. Stieger, *J. Hepatol.*, 2011, **54**, 738–745.
22 J. V. Frangioni, *Curr. Opin. Chem. Biol.*, 2003, **7**, 626–634.
23 L. A. Yannuzzi, *Am. J. Ophthalmol.*, 2011, **151**(5), 745–751.
24 X. Zheng, D. Xing, F. Zhou, B. Wu and W. R. Chen, *Mol. Pharm.*, 2011, **8**, 447–456.
25 H. Wang, X. Li, B. W.-C. Tse, H. Yang, C. A. Thorling, Y. Liu, M. Touraud, J. B. Chouane, X. Liu, M. S. Roberts and X. Liang, *Theranostics*, 2018, **8**, 1227–1242.
26 J. Chen, T. Fan, Z. Xie, Q. Zeng, P. Xue, T. Zheng, Y. Chen, X. Luo and H. Zhang, *Biomaterials*, 2020, **237**, 119827.
27 X. Sun, G. He, C. Xiong, C. Wang, X. Lian, L. Hu, Z. Li, S. J. Dalgarno, Y. W. Yang and J. Tian, *ACS Appl. Mater. Interfaces*, 2021, **13**, 3679–3693.
28 J. Shao, R. Liang, D. Ding, X. Zheng, X. Zhu, S. Hu, H. Wei and B. Wei, *Int. J. Nanomed.*, 2021, **16**, 2897–2915.
29 J. Liu, Y. Yin, L. Yang, B. Lu, Z. Yang, W. Wang and R. Li, *Int. J. Nanomed.*, 2021, **16**, 1473–1485.
30 S. Mindt, I. Karampinis, M. John, M. Neumaier and K. Nowak, *Photochem. Photobiol. Sci.*, 2018, **17**, 1189–1196.
31 P. Zhao, M. Zheng, C. Yue, Z. Luo, P. Gong, G. Gao, Z. Sheng, C. Zheng and L. Cai, *Biomaterials*, 2014, **35**, 6037–6046.
32 T. Lajunen, R. Nurmi, D. Wilbie, T. Ruoslahti, N. G. Johansson, O. Korhonen, T. Rog, A. Bunker, M. Ruponen and A. Urtti, *J. Controlled Release*, 2018, **284**, 213–223.
33 C. Yang, J. Xu, D. D. Yang, X. X. Wang, B. Liu, N. Y. He and Z. F. Wang, *Chin. Chem. Lett.*, 2018, **29**, 1421–1424.
34 E. Jung, J. Lee, L. Jeong, S. Park, M. Lee, C. Song and D. Lee, *Biomaterials*, 2019, **192**, 282–291.

35 Q. Chen, L. Xu, C. Liang, C. Wang, R. Peng and Z. Liu, *Nat. Commun.*, 2016, **7**, 13193.
36 Z. Chen, P. Zhao, Z. Luo, M. Zheng, H. Tian, P. Gong, G. Gao, H. Pan, L. Liu, A. Ma, H. Cui, Y. Ma and L. Cai, *ACS Nano*, 2016, **10**, 10049–10057.
37 B. Liu, C. Li, G. Chen, B. Liu, X. Deng, Y. Wei, J. Xia, B. Xing, P. a. Ma and J. Lin, *Adv. Sci.*, 2017, **4**, 1600540.
38 Z. A. I. Mazrad, P. T. M. Phuong, C. A. Choi, I. In, K. D. Lee and S. Y. Park, *ChemMedChem*, 2018, **13**, 2437–2447.
39 Y. Long, X. Wu, Z. Li, J. Fan, X. Hu and B. Liu, *Biomater. Sci.*, 2020, **8**, 5088–5105.
40 C. Müller, G. Perera, V. König and A. Bernkop-Schnürch, *Eur. J. Pharm. Biopharm.*, 2014, **87**, 125–131.
41 X. Duan, J. Xiao, Q. Yin, Z. Zhang, S. Mao and Y. Li, *Int. J. Nanomed.*, 2012, **7**, 4961–4972.
42 N. Alifu, X. B. Dong, D. Y. Li, X. H. Sun, A. Zebibula, D. Q. Zhang, G. X. Zhang and J. Qian, *Mater. Chem. Front.*, 2017, **1**, 1746–1753.
43 E. Dellacasa, M. Forouharshad, R. Rolandi, L. Pastorino and O. Monticelli, *Mater. Lett.*, 2018, **220**, 241–244.
44 L. J. Liu, W. Liu, G. Ji, Z. Y. Wu, B. Xu, J. Qian and W. J. Tian, *Chin. J. Polym. Sci.*, 2019, **37**, 401–408.
45 P. Arnaldi, L. Pastorino and O. Monticelli, *Int. J. Biol. Macromol.*, 2020, **163**, 393–401.
46 S. Abe and M. Otsuki, *Curr. Med. Chem.: Anti-Cancer Agents*, 2002, **2**, 715–726.
47 M. J. Vicent and R. Duncan, *Trends Biotechnol.*, 2006, **24**, 39–47.
48 M. Qiu, A. Singh, D. Wang, J. Qu, M. Swihart, H. Zhang and P. N. Prasad, *Nano Today*, 2019, **25**, 135–155.
49 W. Lin, C. Li, N. Xu, M. Watanabe, R. Xue, A. Xu, M. Araki, R. Sun, C. Liu, Y. Nasu and P. Huang, *Int. J. Nanomed.*, 2021, **16**, 2775–2787.
50 M. Hou, C. Yan, Z. Chen, Q. Zhao, M. Yuan, Y. Xu and B. Zhao, *Acta Biomater.*, 2018, **74**, 334–343.
51 Q. Hu, K. Wang and L. Qiu, *Colloids Surf., B*, 2021, **197**, 111372.
52 Z. Shi, C. Chu, Y. Zhang, Z. Su, H. Lin, X. Pang, X. Wang, G. Liu and W. Li, *J. Biomed. Nanotechnol.*, 2018, **14**, 1934–1943.